A framework for the analysis of scattering from complex objects using locally smooth surface parametrizations and the generalized method of moments

N. V. Nair[a,*], B. Shanker[a,b], L. Kempel[a]

[a]*Department of Electrical and Computer Engineering, Michigan State University, East Lansing, MI 48824, USA.*
[b]*Department of Physics and Astronomy, Michigan State University, East Lansing, MI 48824, USA.*

arXiv:1107.3526v1 [physics.comp-ph] 18 Jul 2011

Keywords: Generalized method of moments, Locally smooth surface parametrizations, Integral equations, Acoustic scattering

1. Introduction

Integral equation methods for the solution of partial differential equations in engineering have seen a surge of applicability following the development of the fast multipole based methods [1, 2] that reduced the computational cost from $O(N^2)$ to $O(N)$, where N is the number of degrees of freedom. The range of practical problems that can be solved using integral equations has brought to the forefront an interesting array of challenges such as the development of well conditioned formulations, rapidly convergent iterative schemes and accurate basis function representations. There has been a slew of work in these directions in the electromagnetic community, including the development of Calderon pre-conditioners [3], loop star basis function schemes [4] and higher order and singular basis functions [5, 6]. Over the past years, the authors have worked on the design of a basis function framework for integral equations called the generalized method of moments, that addresses some of these issues. This technique allowed for (i) the easy inclusion of arbitrary functions in the basis space, (ii) the arbitrary mixing of different types and orders of basis functions and (iii) non-conformal meshes within a Galerkin method of moments setting. However, in addition to these, important, "solver-side" issues, significant challenges arise on the side of constructing geometric models that represent the problems under analysis.

The surface integral equation schemes currently in use, almost always start from some parametric description of the scatterer surface. Thus the first step to any analysis is the construction of a mesh. In cases where a smooth, invertible, mapping can be found from the geometry to a canonical shape in a convenient coordinate system, this process reduces to meshing the canonical shape. A classic example is when a geometry can be mapped on to a sphere. Meshing a sphere is trivial, and once a spherical mesh is available, the mapping can be used to transform the nodes and the faces (or edges) to the actual geometry. However, this is obviously not possible for any but the simplest possible shapes. Thus for complex, realistic geometries, we are left with two options: (i) divide the geometry into smaller pieces that can be mapped on to canonical geometries and then stitch the respective meshes together at interfaces, or (ii) start from a point cloud description of the geometry and construct a mesh from this point cloud. The first method comes with several disadvantages, the most prominent being that neither the subdivision nor the stitching process can be automated. We will concentrate here, on the second procedure, namely the construction of a surface mesh from a three dimensional point cloud.

While in two dimensions, the problem is well studied and solutions are available in $O(NlogN)$ time or better, [7–11], given an arbitrary point cloud in 3D, reconstructing a surface mesh is a highly under-determined, and therefore much harder, problem. One of the more prominent algorithms in use is the ball pivoting algorithm (BPA) [12]. While the BPA is largely successful for uniformly dense meshes without noise, it has several known issues when the geometry has very large or very small curvatures. This is particularly difficult when there are either (i) multiple holes

*Department of Electrical and Computer Engineering, Michigan State University, East Lansing, MI 48824, USA. Ph. 517-432-6416, nairn@msu.edu

Email addresses: nairn@msu.edu (N. V. Nair), bshanker@egr.msu.edu (B. Shanker), kempel@egr.msu.edu (L. Kempel)

in the geometry or (ii) when there are very thin features on the geometry; both of which is true of many realistic structures.

Even after a mesh is created, most existing integral equation solvers "expect" a reasonably uniform, "clean" mesh. In particular, most solution algorithms have no tolerance for non conformal meshes (where two triangles share just a *part* of an edge) and return very badly conditioned numerical systems when applied to non-uniform meshes. It is worth mention, here, that there exist a class of collocation based methods [13–16] which work directly on point clouds, as opposed to a surface mesh. While these methods work well for smooth surfaces, certain challenges arise from the singularity of the kernel that are not easily overcome. As a result, mesh based scheme, which allow for surface integration, and therefore, reduction in one order of singularity in the integrand, are preferred. In this work we will describe a unified framework that can (i) seamlessly incorporate point clouds and standard mesh primitives such as triangles, quadrilaterals, etc., (ii) construct a locally smooth surface representation starting from these primitives or point clouds, (iv) provide mechanisms to adaptively and automatically adjust the local order and size of this representation (iii) develop arbitrary function spaces on these surface parametrizations (iv) discretize the integral operator using basis functions from these function spaces and (iv) solve the resulting system using Galerkin testing. We will use the problem of acoustic scattering from sound hard objects as a vehicle for describing and validating the technique we present here.

The rest of this paper will proceed as follows: In the next section, we will state, formally, the scattering problem. In section 3 we will describe the construction of the locally smooth surface parametrizations. In the following section, we will detail the construction of the basis function scheme on these surface parametrizations. The specifics of construction of the matrix elements will be elucidated in section 5. Section 6 will present several results that demonstrate the surface reconstruction, validate the basis function framework and showcase several of the advantages of the proposed technique. Finally, section 7 will provide some concluding remarks.

2. Problem Statement

Let D^- denote a rigid scatterer in a homogeneous medium bounded by Ω with a unique, outward pointing normal $\hat{\mathbf{n}}(\mathbf{r})\forall\mathbf{r}\in\Omega$. Consider a velocity field incident on this scatterer denoted by $\mathbf{v}^i(\mathbf{r})$. This generates a scattered velocity field given by $\mathbf{v}^s(\mathbf{r})$ and we define the total velocity as $\mathbf{v}^t(\mathbf{r}) \doteq \mathbf{v}^i(\mathbf{r}) + \mathbf{v}^s(\mathbf{r})$. These fields can be represented by an equivalent potentials $\phi^\zeta(\mathbf{r})$, $\zeta\in\{i,s,t\}$, where $\mathbf{v}^\zeta\mathbf{r}) \doteq \nabla\phi^\zeta(\mathbf{r})$. Further, the corresponding pressure fields are given by $p^\zeta(\mathbf{r}) \doteq -j\omega\rho_0\phi^\zeta(\mathbf{r})$ where ρ_0 is the density of the ambient medium. The total potential $\phi^t(\mathbf{r}) = \phi^i(\mathbf{r}) + \phi^s(\mathbf{r})$ satisfies the Helmholtz equation and boundary condition given by

$$\begin{aligned} \nabla^2\phi^t(\mathbf{r}) + k^2\phi^t(\mathbf{r}) &= 0 \qquad \forall \qquad \mathbf{r}\in\mathcal{R}^3/D^- \\ \hat{\mathbf{n}}(\mathbf{r})\cdot\nabla\phi^t(\mathbf{r}) &= 0 \qquad \forall \qquad \mathbf{r}\in\Omega. \end{aligned} \tag{1}$$

The Kirchoff-Helmholtz integral theorem relates the scattered potential $\phi^s(\mathbf{r})$ to the total potential as

$$\phi^s(\mathbf{r}) = \int_\Omega d\mathbf{r}\phi^t(\mathbf{r}')\hat{\mathbf{n}}'(\mathbf{r}')\nabla' g(\mathbf{r},\mathbf{r}'), \tag{2}$$

where $g(\mathbf{r},\mathbf{r}') \doteq \exp(-jk|\mathbf{r}-\mathbf{r}'|)/4\pi|\mathbf{r}-\mathbf{r}'|$ and k is the wave number of the incident field. Imposing the condition that the total pressure $p^t(\mathbf{r}) \doteq p^i(\mathbf{r}) + p^s(\mathbf{r}) = 0$ on the surface Ω provides an integral equation for the total potential, $\phi^t(\mathbf{r})$, given by

$$\phi^i(\mathbf{r}) = \frac{1}{2}\phi^t(\mathbf{r}) - \int_\Omega d\mathbf{r}'\phi^t(\mathbf{r}')\hat{\mathbf{n}}'(\mathbf{r}')\cdot\nabla' g(\mathbf{r},\mathbf{r}'). \tag{3}$$

Further, by imposing that the normal component of the velocity goes to zero on the surface of the scatterer, i.e. $\hat{\mathbf{n}}(\mathbf{r})\cdot\mathbf{v}^t = 0$, $\mathbf{r}\in\Omega$, we obtain the normal derivative of the above integral equation.

$$\hat{\mathbf{n}}(\mathbf{r})\cdot\nabla\phi^i(\mathbf{r}) = \int_\Omega d\mathbf{r}'\phi^t(\mathbf{r}')\hat{\mathbf{n}}(\mathbf{r})\cdot\nabla\hat{\mathbf{n}}'(\mathbf{r}')\cdot\nabla' g(\mathbf{r},\mathbf{r}'). \tag{4}$$

For ease of representation in the rest of this paper, we will define two integral operators $\mathcal{K}$ and $\mathcal{T}$ as

$$\mathcal{K}\circ[\phi(\mathbf{r})] \doteq \frac{1}{2}\phi(\mathbf{r}) - \int_\Omega d\mathbf{r}'\phi(\mathbf{r}')\hat{\mathbf{n}}'(\mathbf{r}')\cdot\nabla' g(\mathbf{r},\mathbf{r}') \tag{5a}$$

and

$$\mathcal{T} \circ [\phi(\mathbf{r})] \doteq \int_\Omega d\mathbf{r}' \phi(\mathbf{r}') \hat{\mathbf{n}}(\mathbf{r}) \cdot \nabla \hat{\mathbf{n}}'(\mathbf{r}') \cdot \nabla' g(\mathbf{r}, \mathbf{r}') \tag{5b}$$

The two integral equations in (3) and (4) can be combined using a parameter α as follows, in a formulation that guarantees uniqueness in the solution $\phi^t(\mathbf{r})$ [17];

$$\alpha \phi^i(\mathbf{r}) + (1-\alpha) \hat{\mathbf{n}}(\mathbf{r}) \cdot \nabla \phi^i(\mathbf{r}) = \alpha \mathcal{K} \circ [\phi^t(\mathbf{r})] + (1-\alpha) \mathcal{T} \circ [\phi^t(\mathbf{r})], \tag{6}$$

where $\alpha \in (0, 1)$. Typical solution of equation (6) proceeds by representing the unknown potential $\phi^t(\mathbf{r})$ in a set of spatial basis functions, i.e. $\phi^t(\mathbf{r}) = \sum_n a_n \phi_n(\mathbf{r})$, where a_n are unknown coefficients. Substituting this representation into (6) and Galerkin testing using the same set of basis functions results in a matrix system of the form

$$\underline{\underline{\mathrm{Z}}}\underline{\mathrm{a}} = \underline{\mathrm{f}}, \tag{7}$$

where

$$\underline{\underline{\mathrm{Z}}} = \left[Z_{i,j}\right] \doteq \int_{\Omega \cup \Omega_i} d\mathbf{r} \phi_i(\mathbf{r}) \mathcal{X} \circ [\phi_j(\mathbf{r})], \tag{8}$$

and $\mathcal{X} \doteq \alpha \mathcal{K} + (1-\alpha)\mathcal{T}$, $\underline{\mathrm{a}} \doteq [a_i]$ and

$$\underline{\mathrm{f}} = [f_i] \doteq \int_\Omega d\mathbf{r} \phi_i(\mathbf{r}) \phi^i(\mathbf{r}). \tag{9}$$

Typical method of moments solutions employ polynomial basis functions defined on a simplicial tessellation of the geometry Ω. These basis spaces rely heavily on mapped polynomial functions defined on tessellations of the geometry. However, in the case of complex structures, the construction of such a tessellation is often very difficult and/or costly. Even when such a tessellation is constructed, it often results in a highly irregular mesh which, in turn, results in a matrix system that is ill conditioned and therefore difficult to solve. In this paper, we will take a different approach to the construction of local "patches" on the geometry and the design of basis functions on these patches.

The basis function framework used here was first introduced by the authors previously in [18–21] using piecewise flat domains for the definition of the basis functions. In this work, we will demonstrate the construction of GMM basis functions using a locally smooth approximation to the scatterer surface. Due to space constraints, we will present the novel surface approximation in detail while we will restrict our presentation of the basis functions and the GMM technique itself to a brief outline of the method and direct the reader to the authors' previous works, [20, 21], for further details. In the following section we detail the construction of these locally smooth surface approximations.

3. Construction of Locally Smooth Surface Parametrizations

To construct basis functions, we first need to construct a local parameterization of the surface. The domains of support of these basis functions that we will describe are a set of overlapping patches that cover the surface of the scatterer. A procedure to construct these locally smooth overlapping patches will be described in detail in the rest of this section.

3.1. Construction of GMM domains

We begin by partitioning the domain Ω into patches Ω_i that overlap and completely cover the domain. To this end, assume that the domain Ω is described by a set of nodes $\mathcal{N}_L = \cup_{i=1}^{L} \{\mathcal{N}_i\}$, a connectivity map consisting of primitives $\Delta_N = \cup_{n=1}^{N} \{\Delta_n\}$, and finally a unique set of normals $\hat{\mathbf{n}}_i$ at these points. Each primitive is defined by a collection of nodes $\Delta_n \doteq \left\{\mathcal{N}_{n,j}\right\}_{j=1}^{j=m_n} \subset \mathcal{N}_L$. In the case of a standard, flat, triangulation, this will reduce to $m_n = 3\ \forall n$, i.e. all the primitives are triangles. To define locally smooth GMM patches, we first start from a collection of triangles that share a node $\mathcal{N}_i$. This collection will be denoted by Ω_i.

Note, that these collections can also be equivalently described starting from a meshless point-cloud framework as opposed to a triangulation. For the "first-generation" GMM scheme described in [20, 21], these piece-wise flat patches are directly used as domains of support for the GMM basis functions. Such a piece-wise flat patch is illustrated in Figure 1. To construct a locally smooth approximation to Ω starting from these patches, we first define a patch normal, a projection plane and a notion of local convexity for each patch Ω_i, as follows.

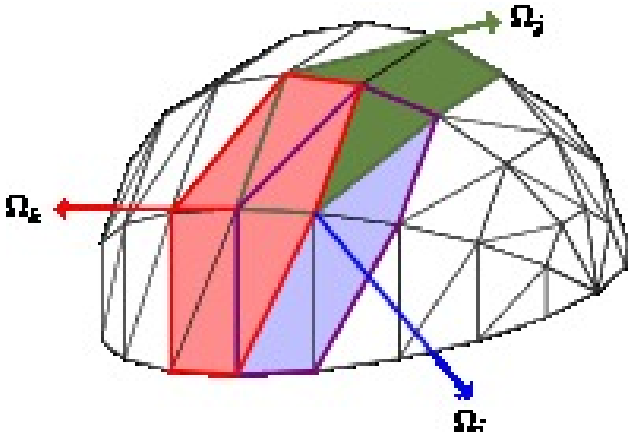

Figure 1: Piecewise flat GMM patches ($\{\Omega_i\}$) shown as shaded region. The patches are constructed as a set of triangles joined at a node.

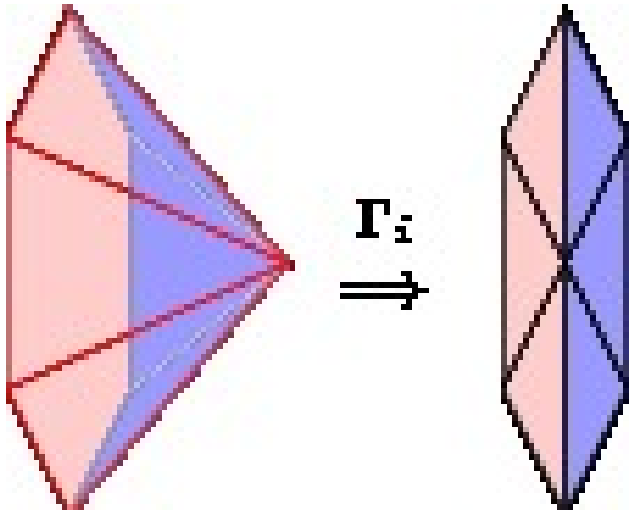

Figure 2: Construction of a projection plane (Γ_i) from a GMM patch comprising of standard triangulations.

Definition 1. *Local Convexity*

Given a patch Ω_i, centered around a point $\mathcal{N}_i \doteq \mathbf{r}_i$ and a parameter ε, the average normal for the patch Ω_i is defined as

$$\hat{\mathbf{n}}_{i,\varepsilon} = \frac{1}{m_n} \sum_{k=1}^{m_n} \hat{\mathbf{n}}(\mathbf{r}_k), \tag{10}$$

where $\mathbf{r}_k$ are points chosen on each of the member primitives such that $\mathbf{r}_k \subset \Omega_i \cap \Delta_k$ and $\|\mathbf{r}_k - \mathbf{r}_i\|_2 \leq \varepsilon$.

Further, a projection plane for patch Ω_i is defined as the plane passing through $\mathbf{r}_i$ and normal to $\hat{\mathbf{n}}_{i,\varepsilon}$. Let Γ_i be the projection of Ω_i on this plane. We denote the projection of a point $\mathbf{r} \in \Omega_i$ to the plane Γ_i by $\mathbf{r}'$. Given the above, we define the patch Ω_i to be locally convex *if we can find some ε such that, $\forall \mathbf{r} \in \Omega_i$ and for $\mathbf{r} \neq \mathbf{r}_i$, $(\mathbf{r} - \mathbf{r}_i) \cdot \hat{\mathbf{n}}_{i,\varepsilon} \geq 0$.*

In other words, a locally convex patch is one for which we can find a projection plane such that the entire patch lies on one side of the plane. Figure 2 shows the construction of the patch normal and projection plane for a locally convex patch. For a locally convex patch, we can define a local coordinate system containing the projection plane and the patch normal, as follows

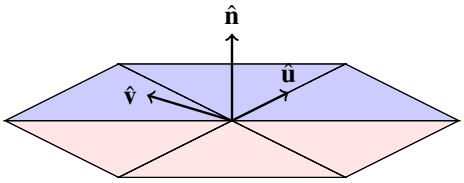

Figure 3: Construction of a local coordinate system.

Figure 4: Construction of a locally smooth parameterization.

Definition 2. *Patch coordinate system*

For a locally convex patch Ω_i, we choose a point $\mathbf{r}'_m$ such that $|\mathbf{r}'_m - \mathbf{r}'_i| > 0$, on Γ_i and define the following local co-ordinate system $\{\hat{\mathbf{u}}, \hat{\mathbf{v}}, \hat{\mathbf{w}}\}_i$ and corresponding projections $\mathbf{u}(\mathbf{r}), \mathbf{v}(\mathbf{r}), \mathbf{w}(\mathbf{r})$ for any point $\mathbf{r} \in \Omega_i$ as $\hat{\mathbf{w}} \doteq \hat{\mathbf{n}}_i$, $\hat{\mathbf{u}} \doteq \left(\mathbf{r}'_m - \mathbf{r}'_i\right)/|\mathbf{r}'_m - \mathbf{r}'_i|$, $\hat{\mathbf{v}} \doteq (\hat{\mathbf{n}} \times \hat{\mathbf{u}})/|\hat{\mathbf{n}} \times \hat{\mathbf{u}}|$, $\mathbf{u}(\mathbf{r}) = \mathbf{r}' \cdot \hat{\mathbf{u}}$, $\mathbf{v}(\mathbf{r}) = \mathbf{r}' \cdot \hat{\mathbf{v}}$ and $\mathbf{w}(\mathbf{r}) = \mathbf{r}' \cdot \hat{\mathbf{w}}$.

Finally, we can use the above definitions to generate a polynomial map whose domain is the projection Γ_i, described by the local coordinates $(\mathbf{u}, \mathbf{v})$ and whose range is a smooth surface. This mapping will become the "generator" for the locally smooth surface and is called the GMM surface map.

Definition 3. *GMM surface map*

Given a locally convex patch Ω_i and a corresponding coordinate system $\{\hat{\mathbf{u}}, \hat{\mathbf{v}}, \hat{\mathbf{w}}\}$, we can define a polynomial $\mathcal{P}_i^g(\mathbf{u}, \mathbf{v})$ in two variables $(\mathbf{u},\mathbf{v})$ complete to order g, by its coefficient vector $\mathcal{C}_i^g \doteq \left[c_0, \ldots c_{(g+1)(g+2)/2}\right]$. The polynomial $\mathcal{P}_i$ (and corresponding $\mathcal{C}_i^g$), that minimizes the norm $\min_{\mathbf{r}\in\Omega_i} \left\|\mathcal{P}_i^g(\mathbf{u}(\mathbf{r}), \mathbf{v}(\mathbf{r})) - \mathbf{w}(\mathbf{r})\right\|_2$ can be used to define a transformation $\mathcal{L}_i^g$ from Ω_i to Λ_i, given by

$$\mathcal{L}_i^g(\mathbf{r}) : \Omega_i \rightarrow \Lambda_i \doteq \mathbf{u}\hat{\mathbf{u}} + \mathbf{v}\hat{\mathbf{v}} + \mathcal{P}_i^g(\mathbf{u}, \mathbf{v})\hat{\mathbf{w}}. \tag{11}$$

Λ_i forms an order-p smooth, least-squares approximation to Ω_i. This transformation is called the GMM surface map. The patch Λ_i is called a GMM patch of order g.

Figure 4 demonstrates the construction of a locally smooth approximation of the piecewise flat patch described earlier.

3.2. Properties of the GMM Surface Map

Here we list some of the properties of the GMM surface maps that make it uniquely suited to the definition of scalar and vector GMM basis functions.

3.2.1. Smoothness and error convergence

The GMM surface map defined above, provides a continuous surface normal defined by $\hat{\mathbf{m}}_i(\mathbf{r}) \doteq \partial_u \mathcal{L}_i^g(\mathbf{r}) \times \partial_v \mathcal{L}_i^g(\mathbf{r})$ for all $\mathbf{r} \in \Lambda_i$. The construction of the locally smooth GMM patches is illustrated in Figure 5a. The figure demonstrates the construction of two sample patches starting from the triangulation of various parts of a sphere. The figure shows the smooth patches (Λ_i) along with the piece-wise smooth equivalents (Ω_i). The use of the least squares minimization procedure implies that the order of smoothness of the map (p) is automatically chosen depending on an error metric, as opposed to being set (by a user) a-priori. This is illustrated in Figure 14b.

The figure shows the error in the norm $\|\hat{\mathbf{m}}(\mathbf{r}) - \hat{\mathbf{n}}(\mathbf{r})\|_2$ as a function of the order p, for various surfaces, of the form $x^{p_0} + y^{p_0} + z^{p_0} = c$ for a constant c and order parameter p_0. In each case, the surface is first approximated using a

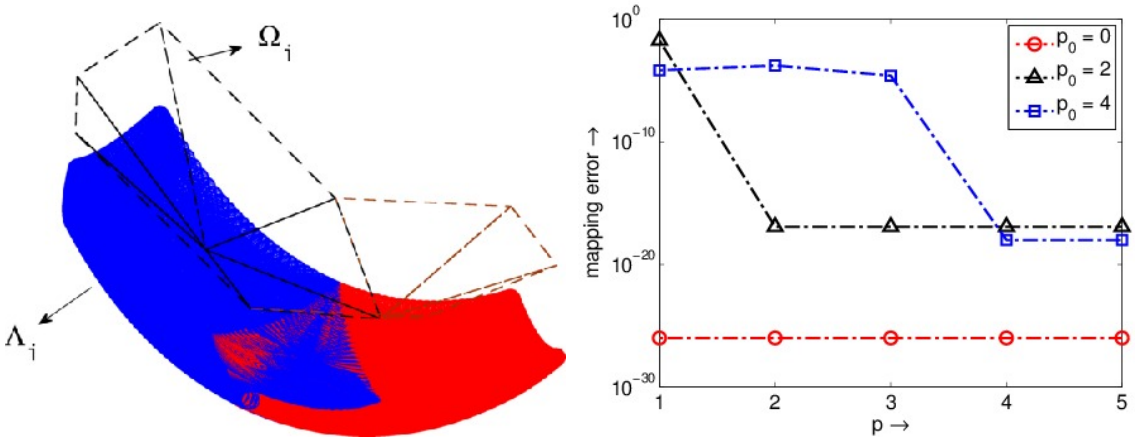

(a) Locally smooth overlapping patches constructed from piecewise smooth patches

(b) Convergence of error in normal for surface approximation

Figure 5: Construction and convergence of locally smooth surfaces

standard piecewise flat triangulation and then GMM patches Ω_i are constructed from these triangles. A locally smooth patch Λ_i is then defined for a given order p and the error in the norm is computed. The error convergence in shown for three surfaces, a flat surface (represented as $p_0 = 0$, a piece of a spherical surface $p_0 = 2$ and a surface with $p_0 = 4$. As can be seen from the figure, the error in each case drops to machine precision once the mapping order reaches a critical value. This provides a naturally adaptive mechanism for the choice of surface order.

3.3. Error definitions and convergence metrics

For each locally smooth surface, constructed above, $\Lambda \doteq \bigcup_i \Lambda_i$, we define an error metric, suited to the definition of surface functions $\mathbf{j}(\mathbf{r}) \in H^{1/2}(\Omega)$ as follows

Definition 4. *Given a surface approximation Λ to a true surface Ω_q, the surface approximation error is defined as*

$$\varepsilon_\nabla = \frac{1}{N}\sum_i \left\| \Pi_i(\mathbf{r})\hat{\mathbf{n}}_{\Omega_q}(\mathbf{r}) - \hat{\mathbf{n}}_{\Lambda_i}(\mathbf{r}) \right\|_2 ; \varepsilon_{1/2} = \frac{1}{N}\left(\sum_i \left\| \int_{\Omega_q} d\mathbf{r}\, \Pi_i(\mathbf{r}) t(\mathbf{r}) - \int_{\Lambda_i} d\mathbf{r}\, t(\mathbf{r}) \right\|_2 \right) + \varepsilon_\nabla \tag{12}$$

where $t(\mathbf{r})$ is any test function and $\hat{\mathbf{n}}_{\Omega_q}(\mathbf{r})$ and $\hat{\mathbf{n}}_{\Lambda_i}(\mathbf{r})$ are surface normals to Ω_q and Λ at $\mathbf{r} \in \Omega_q$ and $\mathbf{r} \in \Lambda_i$ respectively; $\Pi_i(\mathbf{r})$ is defined by

$$\Pi_i(\mathbf{r}) = \begin{cases} 1 & \forall \mathbf{r} \in \Omega_q\big|_{\Omega_{qi}} \\ 0 & else \end{cases} \tag{13}$$

Figure 6 demonstrates the convergence of this error on the surface of a sphere of radius $1m$. In order to study convergence, a locally smooth parametrization is constructed starting from a two different point clouds. The first $p_{tri} = 1$, is a cloud of points corresponding to a first order triangulation of the sphere with average edge length $0.1m$. The second $p_{tri} = 2$, is a second order triangulation, with the same average edge length. The errors ε_∇ and $\varepsilon_{1/2}$ are examined as a function of the polynomial order of the patch. As is clear from the image, the error converges very rapidly with the order of the local parametrization.

3.3.1. Local derivatives and continuity of functions

In order to estimate the smoothness of the surface description generated in the above scheme, we study the behavior of surface gradient tensors of a scalar function $\phi(\mathbf{u}, \mathbf{v})$ defined on the projection. As a first step towards this, given the GMM surface map $\mathcal{L}_i^g(\mathbf{r})$, we denote its first metric tensor by

$$\underline{\mathbf{G}}_i \doteq \begin{bmatrix} g_{11} & g_{12} \\ g_{21} & g_{22} \end{bmatrix} \doteq \begin{bmatrix} \partial_u \mathbf{r} \cdot \partial_u \mathbf{r} & \partial_u \mathbf{r} \cdot \partial_v \mathbf{r} \\ \partial_u \mathbf{r} \cdot \partial_v \mathbf{r} & \partial_v \mathbf{r} \cdot \partial_v \mathbf{r} \end{bmatrix}. \tag{14}$$

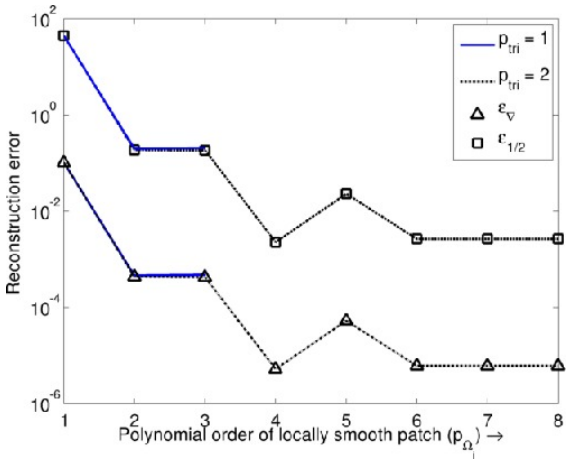

Figure 6: Convergence of surface error metrics with surface patch order

The corresponding surface differential element is denoted by

$$dS \doteq \sqrt{g_i} du dv, \tag{15}$$

where $g_i \doteq det(\underline{\mathbf{G}}_i)$, the determinant of the metric tensor. Each term in the tensor can be defined in terms of the polynomial $\mathcal{P}_i^g(\mathbf{u}, \mathbf{v})$ as

$$\begin{aligned} \partial_u \mathbf{r} &= \hat{\mathbf{u}} + \partial_u \mathcal{P}_i^g(\mathbf{u}, \mathbf{v}) \hat{\mathbf{w}}, \\ \partial_u \mathbf{r} &= \hat{\mathbf{v}} + \partial_v \mathcal{P}_i^g(\mathbf{u}, \mathbf{v}) \hat{\mathbf{w}}. \end{aligned} \tag{16}$$

Given a scalar function $\phi(\mathbf{u}, \mathbf{v})$ defined on the projection plane Γ_i, the surface gradient of the function on Λ_i is given by

$$\nabla_s \phi \doteq g_{11} \partial_u \phi \, \partial_u \mathbf{r} + g_{12} \partial_u \phi \, \partial_v \mathbf{r} + g_{21} \partial_v \phi \, \partial_u \mathbf{r} + g_{22} \partial_v \phi \, \partial_v \mathbf{r}. \tag{17}$$

Higher order derivative tensors on the surface can be described in a similar manner.

From the definition of the surface gradient above, it is clear that any function $\phi(\mathbf{r})$ defined on a gmm patch Λ_i of order g that supports p derivatives on $(\mathbf{u}, \mathbf{v})$ with $p \leq g$ will support at least p surface derivatives on the smooth patch Λ_i. This result implies that, defining a function of order p on the smooth GMM patch Λ_i is equivalent to defining a corresponding function on the projection plane Γ_i. This provides an important tool for the definition of the GMM basis functions as described below.

4. Definition of GMM basis functions

The next step is the development of basis functions in each of the above patches. Consistent with the central theme of the GMM framework, we would like to permit different orders of polynomials or even different functions to be defined on adjacent patches. It has been shown, in the context of finite element methods, that this can be achieved using a product of two functions; (i) a partition of unity (PU) function that provides continuity of the order of this function across overlapping patches and (ii) a higher order function that determines the quality of approximation within a patch [20, 21]. In what follows, we shall discuss each in turn.

4.1. Definition of partition of unity functions

The PU function is defined as a function that associated with a patch is that it decays to zero at its boundary. We define one such function in each patch. Since a patch overlaps with other patches, at any point in the patch multiple different PU functions will be non-zero. This leads to the next condition, viz., all PU functions that are non-zero in a

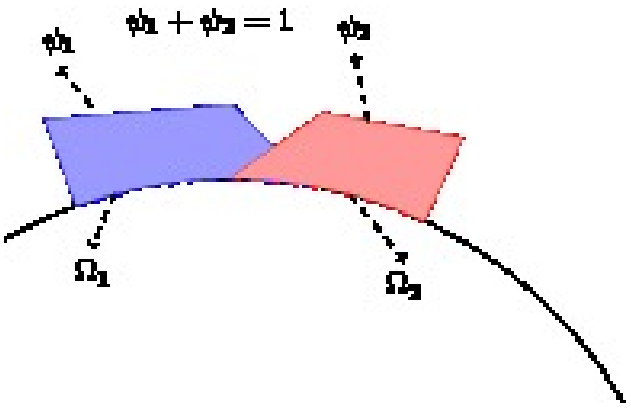

Figure 7: Definition of a GMM patch and partition of unity

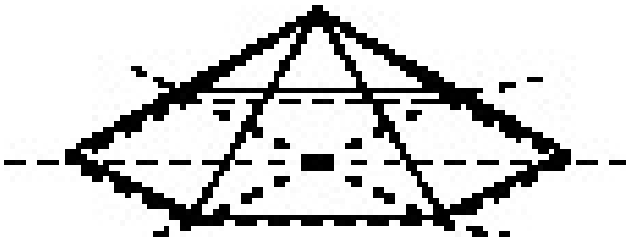

Figure 8: Definition of a pyramid function for partition of unity – $\lambda_{i,j}$

patch add up to one. For illustration, Figure 7 shows two one-dimensional patches and a partition of unity defined on these patches.

To define PU functions on the 3-D GMM patches, we construct a function $\lambda_{i,j}(\mathbf{u}, \mathbf{v})$ which is 1 at the patch center and 0 at the edge of Γ_i. This is achieved using a pyramid function as shown in Figure 8. The partition of unity function is then defined as

$$\psi_i(\mathbf{r}) = \frac{\lambda_{i,j}(\mathbf{r})}{\sum_k \lambda_{k,j}(\mathbf{r})}, \tag{18}$$

where the index k runs through all the patches Ω_k that overlap with Ω_i. It can be verified that this definition ensures that the partition of unity goes to 0 at the ends of the patches and adds up to 1 everywhere on Γ_i. Correspondingly it satisfies these properties on Λ_i.

4.2. Definition of continuous approximation functions

The next step is to define functions that provide higher order approximation of the unknown field in the patch. As before, we start by defining the function on Γ_i. Any function $f(\mathbf{u}, \mathbf{v})$ can be now mapped directly to $f(\mathbf{r})$ on Λ_i. Note, the domain of the approximation function does not need to be identical to the projection of the patch, Γ_i. This is possible as functions defined on these patches are eventually multiplied by a PU function that goes to zero at patch boundaries.

One possible choice of approximation functions can be described using Legendre polynomials of the form $v_i^m(\mathbf{r}) \in \{P_{p_u}(\tilde{u})P_{p_v}(\tilde{v})\}$ where P_q denotes a Legendre polynomial of order q and $p_u + p_v \leq m$ and

$$\begin{aligned} \tilde{u(\mathbf{r})} &\doteq \frac{u(\mathbf{r})}{\max_{\mathbf{r}\in\Lambda_i} u(\mathbf{r})}, \\ \tilde{v(\mathbf{r})} &\doteq \frac{v(\mathbf{r})}{\max_{\mathbf{r}\in\Lambda_i} v(\mathbf{r})}. \end{aligned} \tag{19}$$

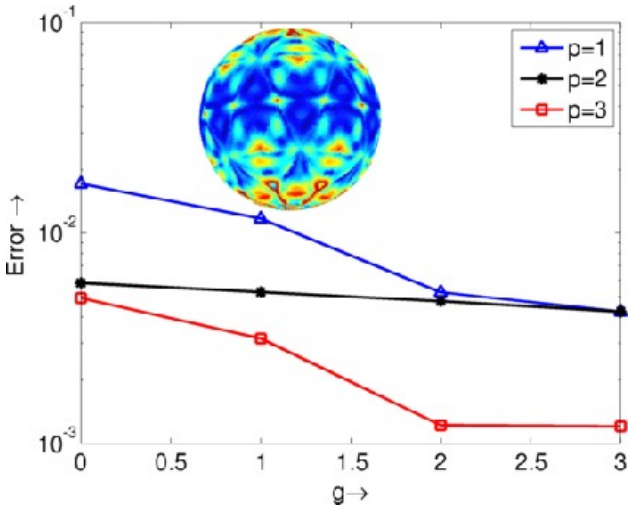

Figure 9: Error convergence for surface functions defined on a sphere. Inset shows a surface plot of the error

Once approximation functions are thus defined, the GMM basis functions are simply products of the approximation function with the partition of unity. That is,

$$\phi_i(\mathbf{r}) \in span_m \{\psi_i(\mathbf{r})\nu_i^m(\mathbf{r})\} \tag{20}$$

Figure 9 shows the convergence of the GMM approximation to a surface function defined on a spherical surface. To test the efficacy of the GMM basis functions, we define a function of the form $f(\mathbf{r}) \doteq f_\theta(\theta,\phi)\hat{\theta} + f_\phi(\theta,\phi)\hat{\phi}$. We then construct local surface parametrizations $\{\Lambda_i\}$ of varying order $g = 1, 2, 3$ to approximate the surface of the sphere and construct basis functions of various orders $p = 1, 2, 3$ on these surfaces. The functions are used to approximate $f(\mathbf{r})$ by setting up

$$\tilde{f(\mathbf{r})} = \sum_i a_i\phi_i(\mathbf{r}) \tag{21a}$$

and solving the matrix system resulting from

$$\int_\Omega d\mathbf{r}\phi_j(\mathbf{r}) \sum_i a_i\phi_i(\mathbf{r}) \approx \int_\Omega d\mathbf{r}\phi_j(\mathbf{r})f(\mathbf{r}) \tag{21b}$$

The coefficients a_i are used to approximate $f(\mathbf{r})$ the norm of the error on the surface is used as a parameter to test convergence. Figure 9 shows the error for $f_\theta = \theta$ and $f_\phi = \phi$ as a function of p and g. As is clear from the figure, the error converges uniformly and logarithmically with both g for each basis function order p. The inset shows a surface plot of the error.

Once the basis functions are defined, the next step is the evaluation of the integrals to construct the matrix elements in $\left[Z_{i,j}\right]$. This will be detailed in the next section.

5. Evaluation of Matrix Elements

The evaluation of the matrix elements in $\left[Z_{i,j}\right]$ involves integrals of the following two forms.

$$\int_{\Lambda_i} d\mathbf{r}\phi_i(\mathbf{r}) \int_{\Lambda_j} d\mathbf{r}'\phi_j(\mathbf{r}')\hat{\mathbf{n}}'(\mathbf{r}') \cdot \nabla' g(\mathbf{r},\mathbf{r}') \tag{22}$$

$$\int_{\Lambda_i} d\mathbf{r}\phi_i(\mathbf{r}) \int_{\Lambda_j} d\mathbf{r}'\phi_j(\mathbf{r}')\hat{\mathbf{n}}(\mathbf{r}) \cdot \nabla\hat{\mathbf{n}}'(\mathbf{r}') \cdot \nabla' g(\mathbf{r},\mathbf{r}'),. \tag{23}$$

The integrals need to be evaluated on patches Λ_i and Λ_j. Using the surface differential element defined in (15), we can map the integral of a function $\Theta(\mathbf{r}, \mathbf{r}')$ on a patch Λ_i to an integral of the function $\Theta(\mathbf{u}, \mathbf{v}, \mathbf{u}', \mathbf{v}')$ on the projections Γ_j and Γ_i as

$$\int_{\Lambda_i} d\mathbf{r} \int_{\Lambda_j} d\mathbf{r}' \phi(\mathbf{r}) = \int_{\Gamma_i} \sqrt{g_i} du dv \int_{\Gamma_j} \sqrt{g_j} du' dv' \; \Theta(\mathbf{u}, \mathbf{v}, \mathbf{u}', \mathbf{v}'). \tag{24}$$

The evaluation of the integrals in (22) and (23) are easily performed using the transformation in (24) and Gaussian quadrature when the patches are well separated from each other. It is observed the Gaussian quadrature rules converge to sufficient accuracy when the centers of the patches are separated by $d > 0.15\lambda$, where λ is the wavelength of the incident field. When the patches are closer to each other, the integrals need to be handled more carefully. We separate the "near" evaluations into two cases.

1. Λ_i and Λ_j are closer than 0.15λ but do not overlap: In this case, the integrals are near singular, but can be evaluated using the techniques described in [20–22].
2. Λ_i and Λ_j overlap : In this case, we split the projections Γ_i and Γ_j into an overlapping section Γ^o and two non overlapping sections Γ_i/Γ^o and Γ_j/Γ^o. Any integral of the form (24) above can be then re-written as follows

$$\begin{aligned} \int_{\Gamma_i} du dv \int_{\Gamma_j} du' dv' = & \int_{\Gamma_i/\Gamma^o} du dv \int_{\Gamma_j/\Gamma^o} du' dv' + \int_{\Gamma_i/\Gamma^o} du dv \int_{\Gamma^o} du' dv' \\ & + \int_{\Gamma_j/\Gamma^o} du dv \int_{\Gamma^o} du' dv' + \int_{\Gamma^o} du dv \int_{\Gamma^o} du' dv'. \end{aligned} \tag{25}$$

The preceding equation contains three double integrals that are near singular and one over Λ^o that is either singular (for (22)) or hyper singular (for (23)). The near singular integrals are handled as in case 1 above. To evaluate the singular integrals, we make the assumption that the overlapping portion is locally flat. This implies that $\sqrt{g} = 1$. In this case, it can be shown that the integral in (22) reduces to 0. The integral of equation (23) on flat patches can be performed by transforming the surface integral into a line integral as described in [17].

6. Results

In this section, we put together the locally smooth parametrization scheme and the GMM basis function formulation to solve a variety of scattering problems. First we will demonstrate the ability of the technique developed in this work to construct locally smooth surface parametrizations. Consider the complex geometries introduced in section 1. Figure 10a shows the surface rendering of a gyroid, mathematically described by the equation $\cos(x)\sin(y) + \cos(y)\sin(x)\cos(z)\sin(x) = 1$. The surface is extremely complex, but, since it is analytically known, obtaining a point cloud, and corresponding normals at each point is relatively simple.Figure 10b shows a point cloud constructed from the gyroid surface description.

Figure 10c shows a standard meshing algorithm (ball reconstruction [23, 24] applied to this gyroid surface mesh. As is clear from the inset (which shows a zoomed-in view of a portion of the mesh), the mesh returned by the standard algorithm has several discrepancies. It is not possible to construct an integral equation solver on this mesh. Further, even if extreme care were to be taken and this mesh cleaned up by hand, it would result in a very non-uniform surface discretization, which in turn would lead to a highly ill-conditioned system of equations, and thereby, inaccuracies in solution.

Finally figure 10d shows the surface parametrization algorithm described in this paper, applied to the gyroid surface. As is clear from the figure, it is possible to obtain a locally smooth parametrization of the surface starting from the simple point cloud, without any of the discrepancies that are caused by the standard algorithm.

Netx, to validate the accuracy and utility of the GMM technique implemented on the locally smooth surfaces, we preform a series of numerical experiments. We begin by presenting results that validate the technique on some canonical (or near-canonical) geometries. The data obtained using the GMM is compared against both analytical data, other integral equation discretization frameworks and the GMM framework itself, evaluated using piecewise flat tessellations of the geometry. Following this, we will present a variety of results that demonstrate (i) $h-$, $p-$ and $hp-$ convergence of the GMM scheme, (ii) the ability of the GMM to mix different orders and classes of basis functions and (iii) its ability to handle complex, multiply connected geometries. In all the cases here, we begin by discretizing

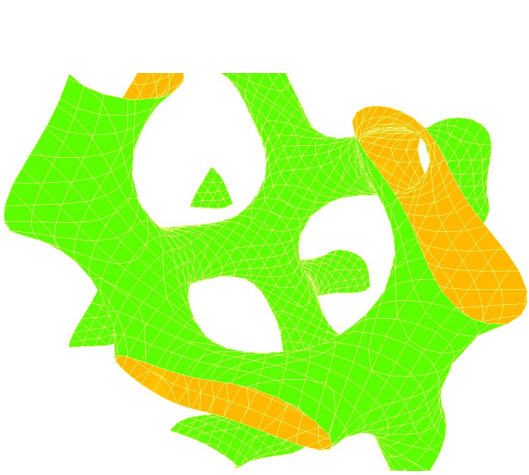

(a) Surface rendering of a gyroid

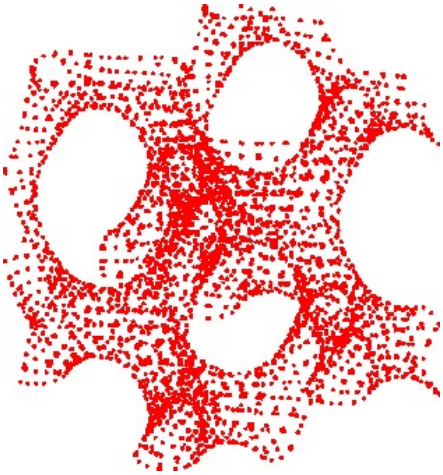

(b) Point cloud for a gyroid

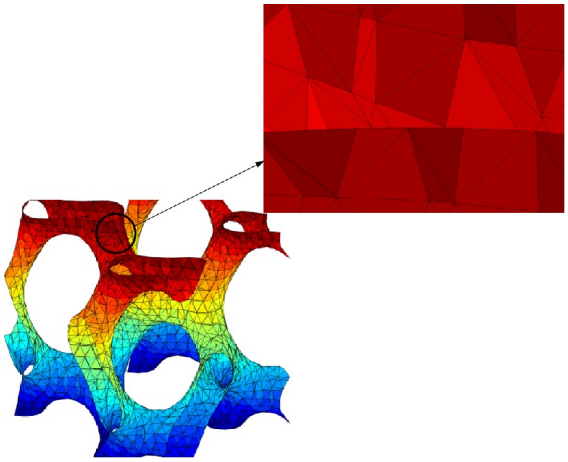

(c) Point cloud for a gyroid

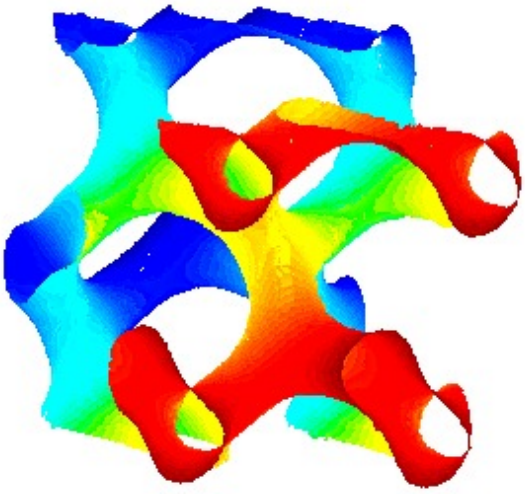

(d) Point cloud for a gyroid

Figure 10: Construction of locally smooth surface representation for a gyroid

the object using a standard triangular meshing scheme with triangles of average edge length corresponding to 0.1λ, where λ is the wavelength of the incident field. The smooth-surface approximations are constructed starting from the point cloud provided by this discretization. In each case, the average diameter of the smallest circle containing the projection of the GMM patch is used as a measure of the size of the patch. In each case, we will use the bistatic scattering cross section (SCS) as a metric for comparison unless otherwise specified. For convenience of notation, we will denote the technique presented in this paper as the GMM-SSA, which will be understood to stand for GMM implemented on "Smooth Surface Approximations", in contrast to the standard GMM scheme presented in [20, 21]. All the cases demonstrated below assume that the test objects are sound-hard and are immersed in a homogeneous medium. Unless explicitly stated, the speed of sound in the ambient medium is assumed to be $343m/s$.

6.1. Validation

6.1.1. Validation against analytical results

First, in figure 12, we validate the locally smooth surface approximation using acoustic scattering from a variety of sound hard obstacles. We first consider scattering from three sphere of radii 1.0λ, 0.2λ and 0.5λ, due to an incident velocity field of frequency $343Hz$. The incident field is a plane wave directed along $-\hat{\mathbf{z}}$. The GMM discretizations, result in $N_{GMM} = 300, 450, 500$ unknowns for each of the spheres when using first order Legendre polynomials p. In each case, the bistatic SCS evaluated at $\phi = 0$ is shown in figure 11a and demonstrates excellent agreement with analytical data, thus validating the SSA-GMM scheme.

Next, we consider the error in backscatter from a sphere of radius 1.0λ. The incident velocity field is a plane wave of frequency $343Hz$ incident along $-\hat{\mathbf{z}}$. We consider the convergence of the relative error in backscatter ($\phi = 0, \theta = 0$) between the GMM scheme and an analytical solution with three different parameters (i) the size of the patches and (ii) the polynomial order of the basis functions (iii) the order of local smoothness of the geometry.

6.1.2. p and g convergence

The first curve in figure 11b shows, for fixed $h = 0.1\lambda$ and $g = 2$, the convergence of the relative error in backscatter with the polynomial order of the basis function p. The corresponding number of unknowns is $N_{GMM} = 320, 640, 960$. Again, the error decreases exponentially with the basis function order, demonstrating the $p-$ convergence of the GMM scheme.

The second curve in figure 11b shows the convergence in relative backscatter error with the order of the geometry (g). The initial patch size is maintained at $h = 0.1\lambda$ and the polynomial order of the basis functions at $p = 2$, and as a result the number of unknowns is constant at $N_{GMM} = 640$. As is clear from the figure, the error decreases exponentially with geometry order. The ability to automatically construct arbitrarily smooth local patches is a unique advantage of the GMM-SSA scheme presented in this paper. The figure clearly demonstrates the utility of constructing such a technique.

6.1.3. Validation against flat GMM

Next, we consider two non-canonical geometries - a NASA almond and a conesphere. Figure 12a shows the bistatic SCS (evaluated at $/phi = 0$) due to scattering from a NASA almond, that fits in a box of size $3.0\lambda \times 1.0\lambda \times 0.1\lambda$. A $343Hz$ velocity field is incident along $-\hat{\mathbf{z}}$ and the almond is discretized using $N_{GMM} = 1700$ unknowns. Figure 12b shows the bistatic SCS (computed at $\theta = \pi/2$) obtained due to a velocity field incident along $\hat{\mathbf{x}}$ on a conesphere with cone-height 2.6λ and sphere radius 0.5λ. The number of unknowns used to discretize $N_GMM = 1078$. The SCS obtained by solution using the GMM-SSA is compared against that obtained using a standard GMM basis set defied on flat patches. Again, the excellent agreement between the SCS validates the GMM-SSA scheme.

6.2. Mixtures of basis functions

The results presented thus far validate the GMM-SSA scheme demonstrate the convergence of the results with the various parameters of the technique. In this section we will present results that demonstrate the ease with which different orders and types of basis functions can be mixed together in the GMM scheme. In traditional basis function schemes, the ability to mix orders of basis functions in neighboring patches is heavily limited by the need to maintain continuity between patches. Typically basis functions have to be restricted to orders of polynomials in order to maintain continuity across patch boundaries. This restricts the classes of basis functions that can be used in the standard $h-$, $p-$ and $hp-$ FEM scheme (and correspondingly for integral equations). However the ability to define arbitrary patches and the construction of the partition of unity scheme enables the use of arbitrary functions in neighboring patches. In this section we present some results that demonstrate this ability.

In the following example, we consider scattering from an ellipsoid of axes 1.0λ, 0.5λ and 0.25λ. The ellipsoid is discretized using patches of average diameter 0.15λ, and the geometry order is maintained at $g = 2$ for all the patches. Polynomial basis functions of order $p = 1$ are used in all patches except patches within 0.1λ of the two ends of the ellipse. In the patches near the end, the basis functions are functions of the form $f(u, v) = \exp -c_i(u^2 + v^2)$, where u, v are the local coordinates on the projection plane, as described in 3. Figure 14b shows the SCS obtained using this scheme with mixed basis functions compared against an SCS obtained using polynomial basis functions everywhere, and one using radial basis functions everywhere. Two sets of SCS's are obtained, one each due to a plane

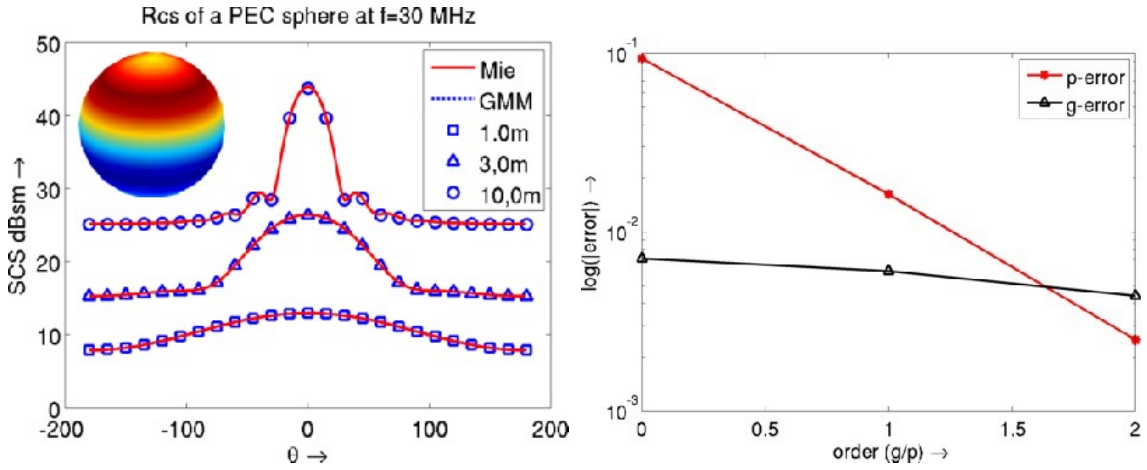

(a) SCS due to scattering from spheres of varying radii $(0.2m, 0.4m, 1.0m)$

(b) Convergence of error in backscatter

Figure 11: Validation results for the GMM

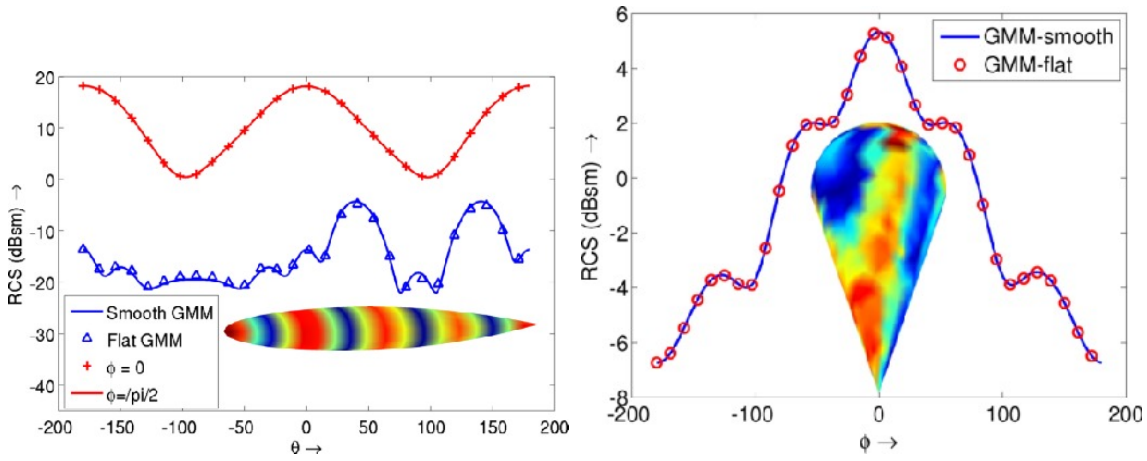

(a) SCS due to scattering from a NASA almond $(3.0\lambda \times 1.0\lambda \times 0.1\lambda)$

(b) SCS due to scattering from a cone-sphere $(2.6\lambda \times 0.5\lambda)$

Figure 12: Validation results for the GMM - comparison against flat GMM: incident field along $\hat{\mathbf{z}}$ for almond, and $\hat{\mathbf{x}}$ for conesphere. The RCS evaluated at $\phi = 0$ for almond and $\theta = 0$ for cone-sphere.

wave incident along $\hat{\mathbf{z}}$ and along $\hat{\mathbf{x}}$ and are evaluated at $\phi = 0$, and $\theta = \pi/2$, respectively. The ability to easily mix different classes of basis functions is a unique capability of the GMM scheme.

6.3. hp-adaptivity

Finally we utilize the flexibility of the GMM (and correspondingly GMM-SSA) scheme to study the $hp-$ convergence of the SCS due to scattering from an ogive of size $10m \times 2m \times 10m$. In each of the cases that follows, the SCS is obtained due to a plane wave incident along $-\hat{\mathbf{z}}$, of frequency $343Hz$. The bistatic SCS is evaluated at $\phi = 0$. To obtain a reference, the ogive is discretized at $h = 0.05\lambda$ everywhere and the SCS is computed using GMM basis functions of polynomial order $p = 1$ defined on this piece-wise flat tessellation resulting in $N_{GMM} = 8406$ unknowns. This is compared against the following different discretizations. To simplify the test, in each of the following cases, the order of the geometry is maintained at $g = 2$ in the smooth areas, $g = 4$ near the ends of the ogive (within 0.25λ of the end) and $g = 7$ for the two patches near the tips. First, theogive is discretized using patches of size 0.25λ in the

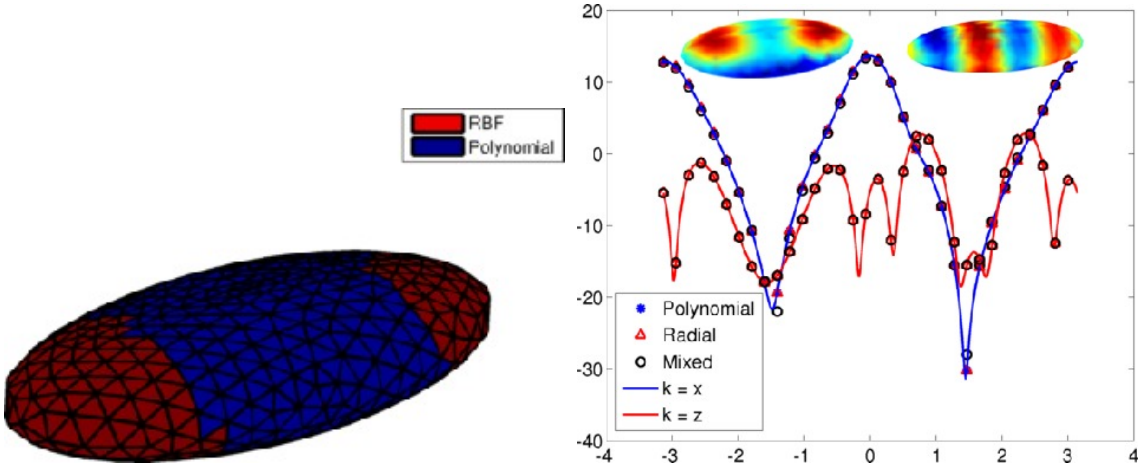

(a) Initial starting mesh for ellipsoid (b) SCS comparison using multiple basis functions

Figure 13: SCS computed using mixed order basis functions on surface of an ellipsoid

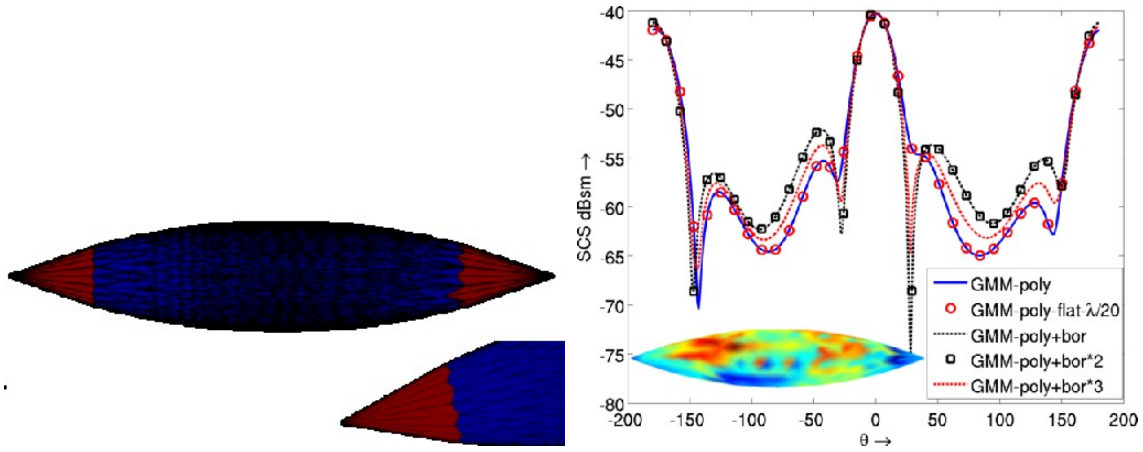

(a) Initial point distribution on ogive (b) Surface currents and SCS comparison

Figure 14: Construction of locally smooth surfaces

smooth areas and 0.1 near the tips (patches within a sphere of 0.2λ near the tips). Basis functions of order $p = 1$ are used in the smaller patches and $p = 2$ in the larger patches. This case is referred to in Figure 14a as $hp - 1$. In the next test, the tip of almond is discretized at 0.1λ, the region near the smooth end of the almond (patches within 0.2λ of the smooth end) is discretized at 0.15λ and the central, smooth portion is discretized at 0.25λ. Basis functions of polynomial order $p = 1$, $p = 2$ and $p = 3$ are used in each of the areas respectively. This case is referred to as $hp - 2$. The number of unknowns is $N_{GMM} = 1156, 1455$ respectively. The agreement of the three SCS shown in Figure 14a demonstrates the easy hp convergence of the GMM-SSA scheme.

7. Conclusion

In this paper we have presented an application of the Generalized method of moments to the discretization of scalar integral equations. Most importantly a mechanism has been described for the construction of locally smooth surface approximations to the scatterer surface. We have shown that these surface approximations can be automatically

constructed from either a regular tessellation of the geometry or a point cloud. We have also shown that the error in these surface approximations converge with surface order. We have implemented a scalar equivalent of the GMM basis function framework on these smooth patches and have presented results on acoustic scattering from sound-hard objects. Several results demonstrating the ability of the GMM scheme to mix basis functions, mix different classes of discretizations and solve for scattering from complex, hitherto untenable geometries have been presented.

References

[1] R. Coifman, V. Rokhlin, S. Wandzura, The fast multipole method for the wave equation: A pedestrian prescription, IEEE Antennas Propagat. Mag. 35 (3) (1993) 7–12.

[2] H. Huang, B. Shanker, A $\wp(n)$ procedure for evaluating the yukawa potential and the ewald summation for peroidic systems, Submited to J. Comp. Phys. (Technical Report Available at https://www.egr.msu.edu/ece/Technicalpapers/).

[3] F. Andriulli, K. Cools, H. Bagci, F. Olyslager, A. Buffa, S. Christiansen, E. Michielssen, A multiplicative calderon preconditioner for the electric field integral equation, IEEE Transactions on Antennas and Propagation 56 (8) (2008) 2398–2412. doi:10.1109/TAP.2008.926788.

[4] G. Vecchi, Loop-Star Decomposition of Basis Functions in the Discretization of the EFIE, IEEE Transactions on Antennas and Propagation 47 (2) (1999) 339–346.

[5] R. D. Graglia, D. R. Wilton, A. F. Peterson, Higher order interpolatory vector bases for computational electromagnetics, IEEE Transactions on Antennas and Propagation 45 (1997) 329–342.

[6] R. Graglia, G. Lombardi, Singular higher order complete vector bases for finite methods, IEEE Transactions on Antennas and Propagation 52 (7) (2004) 1672–1685. doi:10.1109/TAP.2004.831292.

[7] A. Bowyer, Computing dirichlet tessellations, The Computer Journal 24 (1981) 162–166.

[8] D. F. Watson, Computing the n-dimensional tessellation with application to voronoi polytopes, The Computer Journal 24 (1981) 167–172.

[9] A. Fournier, D. Y. Montuno, Triangulating simple polygons and equivalent problems, ACM Transactions on Graphics 3 (1984) 153 – 174.

[10] G. T. Toussaint, A new linear algorithm for triangulating monotone polygons, Pattern Recognition Letters 2 (1984) 155–158.

[11] R. Seidel, A simple and fast incremental randomized algorithm for computing trapezoidal decompositions and for triangulating polygons, Computational Geometry: Theory and Applications 1 (1991) 51–64.

[12] F. Bernardini, J. Mittleman, H. Rushmeier, C. Silva, G. Taubin, The ball-pivoting algorithm for surface reconstruction, Visualization and Computer Graphics, IEEE Transactions on 5 (4) (1999) 349 –359. doi:10.1109/2945.817351.

[13] L. F. Canino, J. J. Ottusch, M. A. Stalzer, J. L. Visher, S. M. Wandzura, Numerical solution of the helmholtz equation in 2d and 3d using a high-order nystrom discretization, Journal of Computational Physics 146 (2) (1998) 627–663. doi:http://dx.doi.org/10.1006/jcph.1998.6077.

[14] S. Gedney, Application of the high-order nystrom scheme to the integral equation solution of electromagnetic interaction problems, Electromagnetic Compatibility, 2000. IEEE International Symposium on 1 (2000) 289–294 vol.1. doi:10.1109/ISEMC.2000.875580.

[15] S. D. Gedney, On deriving a locally corrected nystrom scheme from a quadrature sampled moment method, IEEE Trans. Antennas and Propagat 51 (2003) 2402–2412.

[16] M. Tong, W. Chew, A novel high-order nystrom scheme for 3d boundary integral equations, Antennas and Propagation Society International Symposium, 2005 IEEE 4A (2005) 296–299 vol. 4A. doi:10.1109/APS.2005.1552647.

[17] A. J. Burton, G. F. Miller, The application of integral equation methods to the numerical solution of some exterior boundary-value problems, Proc. Roy. Soc. Lond. A. 323 (1971) 201–210.

[18] N. Nair, B. Shanker, An extension of the Generalized Method of Moments to Higher Order Geometries, in: {\textit To Appear In} Proceedings of the 25th International Review of Progress in Applied Computational Electromagnetics, 2009.

[19] N. Nair, B. Shanker, L. Kempel, An extension of the generalized method of moments to higher order geometries, in: Proceedings of the 25th International Review of Progress in Applied Computational Electromagnetics, 2010.

[20] N. V. Nair, B. Shanker, Generalized method of moments: A novel framework for analyzing scattering from homogeneous dielectric bodies, Journal of the Optical Society of America (A) 28 (2011) 328–340.

[21] N. Nair, B. Shanker, Generalized method of moments: A novel discretization scheme for integral equations, to appear in IEEE Transactions on Antennas and Propagation; technical report available at https://www.egr.msu.edu/ece/technical_papers 26 (6).

[22] B. Shanker, A note on exact evaluation of integrals that are encountered in the MFIE formulations, ECE Technical Reports 1–3.

[23] P. Alliez, L. Saboret, G. Guennebaud, Surface reconstruction from point set, in: CGAL User and Reference Manual, Vol. 3.8, CGAL Editorial Board, 2011, Ch. Surface Reconstruction from Point Sets.

[24] L. Rineau, M. Yvinec, 3d surface mesh generation, in: CGAL User and Reference Manual, 3rd Edition, Vol. 3.8, CGAL Editorial Board, 2011, p. 2011.